EES Catalysis

PAPER

View Article Online
View Journal

Cite this: DOI: 10.1039/d6ey00071a

In situ self-segregation construction of a six-metal LDH/Co–Mn-oxide heterostructure on copper foam for alkaline oxygen evolution

Mingge Zhi,[a] Jinan Niu,*[ab] Chaoyao Yao,[a] Ruixuan Zhang,[a] Shunle Zhou,[a] Sonehra Anjum,[a] Fangfang Liu,[ab] Yihan Ling,[a] Guiqing Liu,[c] Guohua Fan,[d] Arianit A. Reka,[e] Farid Akhtar,[f] Peizhong Feng*[ab] and Hermenegildo Garcia*[g]

Developing efficient and durable oxygen evolution reaction (OER) electrodes for alkaline water electrolysis requires not only catalytically active components but also strong interfacial integration between the catalyst layer and the conductive substrate. Herein, we report a one-step hydrothermal route for constructing a six-metal NiZnCuCoMnFe LDH-based heterostructure directly on copper foam, denoted as M6-LDH/CF. Rather than forming an ideal homogeneous multimetal LDH phase, the synthesis produces an integrated architecture consisting of a six-metal LDH nanosheet framework, segregated Co/Mn-containing oxide or oxyhydroxide surface phases, and a reconstructed Cu/Cu_2O/CuO interfacial region derived from the substrate. Structural analyses indicate that differences in hydrolysis, oxidation, and precipitation behavior among the metal species, together with substrate oxidation under hydrothermal conditions, govern this non-ideal growth pathway. The optimized M6-LDH/CF electrode exhibits overpotentials of 181, 392, and 502 mV at 10, 50, and 100 mA cm^{-2}, respectively, and maintains stable operation at 50 mA cm^{-2} for 100 h. Post-OER XPS further reveals pronounced surface-state evolution, including Cu oxidation, Zn leaching, and the formation of more metal–oxygen–metal coordination environments, indicating that M6-LDH/CF functions as a precatalyst architecture that evolves toward a more oxidized working state during operation. These results suggest that controlled non-ideal *in situ* growth can be used constructively to fabricate integrated multimetal OER electrodes with favorable activity and operational stability in alkaline media.

Received 7th April 2026,
Accepted 9th April 2026

DOI: 10.1039/d6ey00071a

rsc.li/eescatalysis

Broader context

Hydrogen obtained from water using green electricity can become in the near future an energy vector. Alkaline electrolysis is a current mature technology that is ready to be implemented at large scale. In this process, water is reduced to hydrogen (HER) and oxidized to oxygen (OER), becoming split into stoichiometric amounts of the two elements. Efficiency of electrolytic hydrogen generation could be further increased by improving the performance of OER that is the thermodynamic and kinetic most demanding step. Herein we report the spontaneous self-assembling of a high-entropy layered double oxide heterostructure on a copper foam that presents advantage over the current anodic electrode. In a single hydrothermal process from soluble salts, a layered multimetallic (six metals) hydroxide is formed having MnOOH and Co_3O_4 nanoparticles that grows epitaxially on the copper foam metal. This *in situ* growth determines a high electrical connectivity among the components that we have shown that derives from the matching of the crystal phases of Cu/Cu_2O/CuO and multimetallic hydroxide surfaces.

[a] School of Materials Science and Physics, China University of Mining and Technology, Xuzhou 221116, China. E-mail: jinan.niu@cumt.eud.cn, pzfeng@cumt.eud.cn
[b] Jiangsu Key Laboratory for Clean Utilization of Carbon Resources, China University of Mining and Technology, Xuzhou 221116, China
[c] Jiangsu BGRIMM Metal Recycling Science & Technology Co., Ltd, Xuzhou 221121, China
[d] Materials Academy of JITRI, Suzhou 215000, China
[e] Faculty of Natural Sciences and Mathematics, University of Tetova, Tetovo 1200, North Macedonia
[f] Division of Materials Science, Luleå University of Technology, Luleå 97187, Sweden
[g] Instituto de Tecnologia Quimica CSIC-UPV, Universitat Politecnica de Valencia, Valencia 46022, Spain. E-mail: hgarcia@qim.upv.es

1. Introduction

With the accelerating global industrialization and the increasing depletion of fossil fuels, the development of clean, efficient, and sustainable energy conversion technologies has become a core challenge.[1,2] Hydrogen (H_2) produced *via* water electrolysis powered by renewable energy is regarded as an ideal medium for a future green energy system.[3] Specifically, alkaline water electrolysis (AWE) has attracted significant attention because it allows for the deep integration of non-precious metal catalysts.[4] However, the anodic oxygen evolution reaction (OER) is a complex and kinetically sluggish four-electron–proton coupled process.[5] Its high inherent overpotential severely limits the overall energy conversion efficiency. Therefore, developing low-cost, robust, and highly active OER electrocatalysts for alkaline media remains a critical priority in the field of energy chemistry.[6]

Among the various catalyst families explored for alkaline OER, layered double hydroxides (LDHs) have attracted considerable interest because of their flexible metal composition, abundant hydroxyl-rich surfaces, and structural adaptability.[6–10] The brucite-like host layers in LDHs can incorporate different transition-metal cations, offering opportunities to tune the local coordination environment and electronic structure of catalytically active sites.[11] In benchmark systems such as NiFe-LDH, the introduction of additional metal species has often been found to influence the adsorption and desorption behavior of oxygen-containing intermediates, thereby improving OER kinetics.[12,13]

Recently, increasing attention has been paid to compositionally complex multimetal LDH systems for electrocatalysis. Incorporating multiple cations into a single LDH framework may help regulate lattice distortion, local bonding environments, defect chemistry, and interfacial charge transfer.[14–16] Such effects can potentially broaden the range of accessible active motifs beyond those available in conventional bimetallic LDHs. Nevertheless, the behavior of multimetal LDHs prepared directly on conductive substrates is often far more complicated than that of an ideal homogeneous solid solution.[17,18]

During hydrothermal or co-precipitation growth, different transition-metal cations usually exhibit distinct hydrolysis rates, precipitation tendencies, and oxidation behaviors.[19] As a result, the final phase organization is governed not only by precursor composition, but also by kinetic competition among metal species during nucleation and growth.[20] In particular, some cations may preferentially remain in the LDH host lattice, whereas others may undergo partial segregation and form secondary oxide or oxyhydroxide phases. Such non-ideal growth behavior is especially relevant when the catalyst is synthesized *in situ* on an active metallic substrate.[21] In these cases, the substrate does not simply serve as a current collector; instead, it may undergo simultaneous surface oxidation and reconstruction, generating a chemically evolving interfacial layer that further influences catalyst nucleation, adhesion, and electronic coupling.[22,23]

Copper foam is an attractive substrate for the direct growth of OER electrodes because of its high conductivity, porous three-dimensional architecture, and mechanical robustness.[24] However, under alkaline hydrothermal conditions, the copper surface can be partially oxidized into Cu_2O and CuO.[25,26] This interfacial evolution may either hinder or promote the growth of multimetal LDH structures, depending on how lattice matching, nucleation kinetics, and phase segregation develop during synthesis. Despite its likely importance, the coupling between spontaneous phase segregation in multimetal LDH systems and substrate-derived interfacial reconstruction has not yet been sufficiently clarified in relation to OER activity and durability.

To address this issue, we employed a one-step hydrothermal strategy to construct a six-metal NiZnCuCoMnFe LDH-based heterostructure directly on copper foam, hereafter denoted as M6-LDH/CF. Rather than assuming the formation of a perfectly homogeneous multimetallic lattice, this work examines whether differences in cation chemistry and growth kinetics can be utilized to drive the spontaneous formation of an integrated heterostructured electrode. Under optimized conditions, the resulting M6-LDH/CF consists of a six-metal LDH nanosheet framework decorated with segregated Co and Mn containing oxide/oxyhydroxide nanoparticles, together with a reconstructed $Cu/Cu_2O/CuO$ interfacial layer derived from the substrate. By combining structural characterization and electrochemical evaluation, we investigate how this coupled phase organization and interfacial reconstruction affect alkaline OER performance. The results show that M6-LDH/CF exhibits improved catalytic activity and operational stability compared with lower-component LDH controls and a physically coated powder electrode. More importantly, this study suggests that controlled non-ideal growth and spontaneous phase segregation can be used constructively to fabricate integrated multimetal OER electrodes, offering a practical route for the design of integrated alkaline electrocatalytic interfaces (Fig. 1).

2. Experimental

2.1. Materials

All chemical reagents were of analytical grade and purchased from Aladdin (Shanghai, China). Copper foam (CF) with a thickness of 1.5 mm was obtained from Keshenghe Metal Materials Co., Ltd (Suzhou, China). Before use, the CF was sequentially sonicated in acetone, ethanol, and deionized water for 20 minutes each to remove surface contaminants.

2.2. Preparation of CF-supported LDH

In a typical synthesis, 12 mmol of urea, 5 mmol of NH_4F, 0.4 mmol of $Ni(NO_3)_2{\cdot}6H_2O$, 0.4 mmol of $Zn(NO_3)_2{\cdot}6H_2O$, 0.4 mmol of $Co(NO_3)_2{\cdot}6H_2O$, 0.4 mmol of $Cu(NO_3)_2{\cdot}6H_2O$, 0.4 mmol of $Mn(NO_3)_2{\cdot}4H_2O$, and 1 mmol of $Fe(NO_3)_3{\cdot}9H_2O$ were dissolved in 40 mL of deionized water at room temperature and then transferred into a 100 mL Teflon-lined stainless steel autoclave. A pre-treated CF (4 cm × 3 cm) was immersed in the mixed solution. Then, the sealed vessel was heated in an oven at 120 °C for 12 hours. Afterward, the vessel was naturally cooled to room temperature, and the CF-supported LDH was

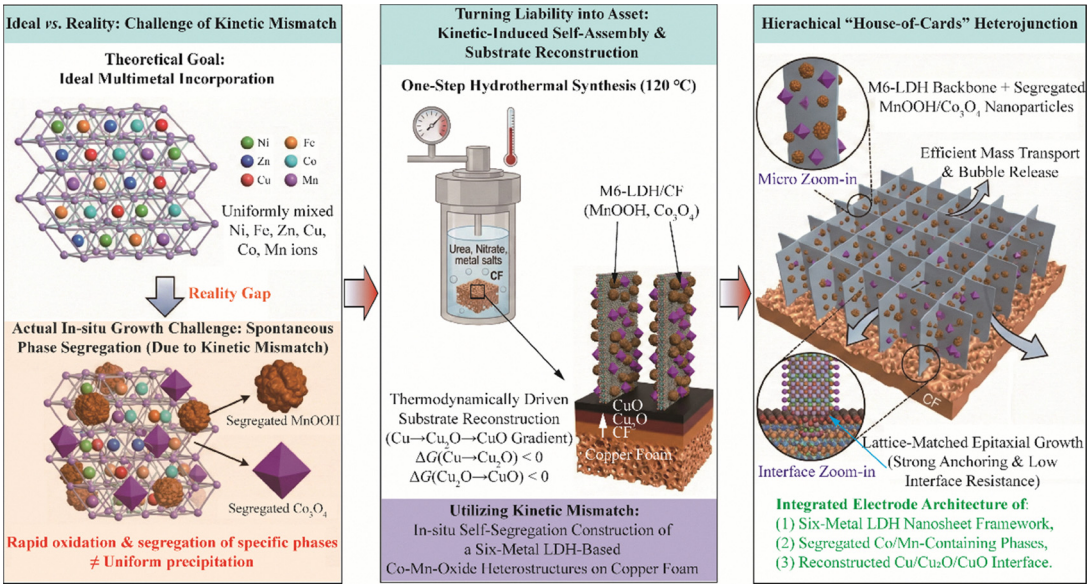

Fig. 1 Schematic illustration of the integrated M6-LDH/CF electrode architecture formation.

removed and rinsed alternately with water and ethanol at least three times. Finally, the obtained sample (Ni : Zn : Co : Cu : Mn : Fe = 0.4 : 0.4 : 0.4 : 0.4 : 0.4 : 1) was vacuum-dried at 60 °C for 12 hours.

In this study, the molar ratio of urea (U) to total divalent cations (M^{2+}) was varied (3, 6, 9, and 12), with M^{2+} concentrations set at 0.025, 0.05, 0.075, and 0.1 mol L^{-1}. The M^{2+}/M^{3+} ratio was maintained at 2 : 1. Synthesis was conducted at temperatures of 80, 100, 120, and 140 °C for durations of 6, 9, 12, and 15 h. Under the optimized parameters, the effect of elemental complexity was investigated. Samples were labeled as M*x*-LDH/CF, where *x* denotes the number of metal components: M2 to M6 represent NiFe, NiCuFe, NiCuZnFe, NiCuZnCoFe, and NiCuZnCoMnFe systems, respectively. For comparison, a six-component powder was synthesized without CF and subsequently loaded onto CF using a Nafion binder, designated as M6-LDH-P/CF. The notation M6 refers to the precursor metal complexity of the synthesis system rather than implying the formation of a perfectly homogeneous six-metal LDH phase.

2.3 Characterization

Morphology analysis was performed on a field emission scanning electron microscope (FESEM, Hitachi SU8220) at an accelerating voltage of 5 kV. All the samples were coated with a thin layer of Au for SEM. Transmission electron morphology and microstructure were observed using field emission transmission electron microscopy (FETEM, JEOL JEM 2100F) at 200 kV, with a Mo grid used to eliminate copper background interference. The TEM sample was prepared by scraping some powder off a copper mesh and then sonicating it in ethanol for 30 seconds. Powder X-ray diffraction (XRD) patterns were recorded on a Bruker X-ray diffraction system (D8 Advance) with Cu-Kα radiation (40 kV, 30 mA). The Raman spectrum was measured by a spectrometer (Horiba, LabRAM HR Evolution) with 785 nm light source and 3 sampling points. X-ray photoelectron spectroscopy (XPS) was carried out by a multitechnique surface analysis system (Thermo Fisher, ESCALAB 250XI). When preparing XPS samples, first cut a 10 × 10 mm CF sample block, rinse it quickly with deionized water, and then dry it under vacuum at 60 °C. To investigate the surface-state reconstruction during the OER process, post-OER XPS analysis was performed on the M6-LDH/CF electrode after the 100 h chronopotentiometry stability test, following the same rinsing and vacuum-drying procedures.

2.4. Electrochemical performance testing

Electrochemical performance testing was conducted using a standard three-electrode system. The working electrode was a CF-supported LDH (1 × 1 cm^2), the counter electrode was a platinum electrode, and the reference electrode was a mercury/mercury oxide electrode. The electrolyte used was 1 M KOH. The apparent OER activity of the sample was studied using linear sweep voltammetry (LSV) polarization curves. The cyclic voltammetry (CV) curves of the samples were tested at different scan rates to further determine the material's double-layer capacitance (C_{dl}). The electrochemically active surface area (ECSA) was estimated based on the measured C_{dl} values, and ECSA-normalized polarization curves were subsequently plotted to evaluate the intrinsic activity contribution. Electrochemical impedance spectroscopy (EIS) was measured to investigate the electron transfer dynamics during the OER process, with a parameter range of 0.01–100 kHz and a voltage selected at 10 mA cm^{-2}. Because transition-metal hydroxide/oxide precatalysts may undergo oxidation/activation prior to the onset of fully developed OER, the polarization-derived overpotentials and Tafel slopes in the low-current region are used mainly for comparative evaluation.

3. Results and discussion

3.1 Optimization of synthesis parameters and morphology control

First, the synthesis process was optimized. Temperature can influence the hydrolysis rate of urea, as well as the crystallization rate and crystal quality of the LDH. At too low a temperature, incomplete crystallization or slow reactions may occur, while too high a temperature may result in rapid growth or cause dissolution side reactions. From the results, temperature had a significant effect on morphology. At 80 °C, needle-like clusters were formed on the substrate, but the coverage was incomplete, indicating that the material was in the early stage of growth (Fig. 2a1). At 100 °C, interconnected sheets formed a three-dimensional network structure, but the sheet morphology was irregular, indicating poor crystallization (Fig. 2a2). At 120 °C, the crystallinity of the nanosheets on the substrate was significantly improved, and the sheets supported each other in a nearly vertical arrangement, forming an open "house-of-cards" structure (Fig. 2a3). However, at 140 °C, the nanosheets on the substrate almost completely disappeared, indicating that excessively high temperatures lead to the dissolution of the sheet structure (Fig. 2a4). The LSV tests of the samples at different temperatures showed that the sample synthesized at 120 °C exhibited the best apparent anodic performance (Fig. 2a5 and Fig. S1), indicating that sufficient crystallinity and an increased number of accessible surface active sites enhance the sample's overall OER performance.

Hydrothermal time also significantly affects the growth integrity, size, and morphology of LDH crystals. Too short a time may result in incomplete grain growth, while too long a time may cause excessive enlargement or structural transformation. The samples obtained at different times under 120 °C all exhibited nearly vertical nanosheet arrays. However, the nanosheets formed after 6 hours were small with thicker sheets (Fig. 2b1). When the time increased to 9 hours, the nanosheets exhibited delamination (Fig. 2b2). After 12 hours, the delamination became more pronounced, showing thinner nanosheets that supported each other (Fig. 2b3), which was due to the Ostwald ripening delamination of the LDH grains.[27] At 15 hours, the nanosheets seemed to undergo recrystallization, presenting thicker and more densely arranged nanosheet arrays (Fig. 2b4). The LSV tests of the samples at different synthesis times showed that the sample synthesized at 120 °C for 12 hours exhibited the best apparent anodic performance (Fig. 2b5 and Fig. S2), corresponding to the optimized exposure of accessible active sites.

The amount of urea directly influences the evolution of the solution pH and the intercalation of carbonate ions, which plays a crucial role in the nucleation, growth, and morphology of LDHs. When the urea ratio is too low, the resulting phase particles are uneven, and the nanosheets do not exhibit significant delamination (Fig. 2c1). However, when the urea ratio is in the higher range of 6 : 1 to 12 : 1, the resulting samples exhibit mutually supporting nanosheets, but the overlap along the sheet normal direction becomes progressively more pronounced (Fig. 2c2–c4). This can be attributed to: (1) enhanced interlayer attraction: the increased concentration of carbonate ions (CO_3^{2-}), derived from urea hydrolysis, promotes electrostatic interactions and hydrogen bonding among brucite-like layers along the *c*-axis; and (2) accelerated kinetics: the rapid release of OH^- induces fast precipitation and Ostwald ripening, driving the thermodynamically favorable transformation from

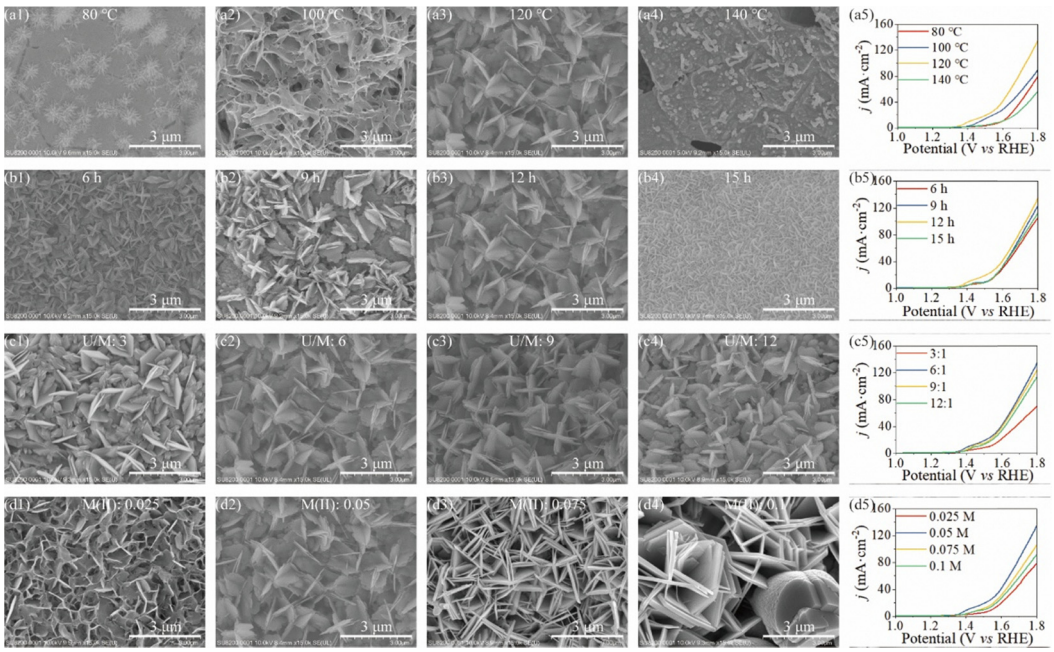

Fig. 2 Summary of optimization results using the single-factor variable method: SEM images and OER performance (LSV curves) of the samples under different (a) reaction temperatures, (b) reaction times, (c) urea/M^{2+} ratios, (d) total M^{2+} concentrations.

high-energy ultrathin sheets to stable, thick stacks. The LSV tests of the samples at different urea amounts show that the sample with a urea/M^{2+} ratio of 6 : 1 exhibits the best apparent anodic performance (Fig. 2c5 and Fig. S3), corresponding to the optimal exposure of accessible active sites.

The total concentration of M^{2+} (or metal ions, due to maintained M^{2+}/M^{3+} ratio) affects the solution''s supersaturation, which in turn influences the nucleation density and growth rate of LDHs, thereby impacting their morphology and coverage. When the M^{2+} ion concentration is 0.025, the sample''s morphology is similar to that in Fig. 2a2, with thin sheets but poor crystallization (Fig. 2d1). As the M^{2+} ion concentration gradually increases from 0.05 to 0.1, the crystallinity, size, and thickness of the samples all increase, and at a concentration of 0.1, even large, irregular particles are formed (Fig. 2d2–d4). The LSV tests of the samples at different M^{2+} ion concentrations show that the sample with an M^{2+} concentration of 0.05 exhibits the best apparent anodic performance (Fig. 2d5 and Fig. S4), further indicating that good apparent electrochemical performance requires sufficient crystallinity and an abundance of accessible surface-active sites to be simultaneously ensured.

The above results indicate that the synthesis process in this study is controllable, with the morphology being highly sensitive to the parameters. The optimal synthesis parameters (120 °C, 12 hours, U/M^{2+} = 6 : 1, M^{2+} concentration = 0.05 M) were determined to yield a uniformly covered, well-crystallized, ultrathin, vertically aligned nanosheet array. All subsequent in-depth characterizations were based on this optimal sample (consistently referred to as M6-LDH/CF in the following discussion).

3.2 Substrate evolution and interfacial reconstruction

From the microscopic morphology of CF (Fig. 3a), it can be seen that the CF exhibits typical metallic copper grain characteristics; some pores are also present near the grain boundaries, which are defects primarily caused during the manufacturing process. After the hydrothermal reaction, a layer of vertically supported ''house-of-cards'' nanosheets grew on the CF surface, almost completely covering the substrate, with the original substrate no longer visible (Fig. 3b). Upon higher magnification, it was observed that the stacking between the LDH nanosheets was relatively loose (Fig. 3c), which facilitates the utilization of accessible interlayer surface active sites and the exchange of OER reactant species. The XRD pattern of CF only shows the characteristic Cu reflection peaks (Fig. 3d), directly corresponding to the SEM morphology (Fig. 3a). In the M6-LDH/CF sample, in addition to the Cu reflection peak, there is a distinct LDH (003) characteristic peak, with no other phase peaks observed, indicating that the newly formed nanosheet array on the CF surface is indeed the LDH phase.

The Raman spectrum of pure CF mainly shows noise peaks, as metallic Cu does not have a first-order Raman-active peak (Fig. S5). After the hydrothermal reaction, in addition to the characteristic peaks of LDH, a typical A_g mode peak of CuO was newly observed (Fig. 3e), indicating that an oxide layer may have formed on the CF surface in the alkaline environment with coexisting nitrate ions, although the amount of CuO formed is relatively small and cannot be clearly detected by XRD. Further XPS narrow scan results of Cu 2p in the M6-LDH/CF sample revealed the coexistence of Cu^{2+} and Cu^{+} oxidation states (Fig. 3f), suggesting that the oxidation process on the CF surface follows a gradual transition from $Cu^0 \rightarrow Cu^+ \rightarrow Cu^{2+}$. In an alkaline environment, the stable compound corresponding to Cu^+ is Cu_2O, but no Cu_2O signal was observed in the Raman spectrum of M6-LDH/CF, likely due to the weak penetration ability of the light source (785 nm) and interference from the surface CuO and LDH. This result indicates that the CF surface may have undergone reconstruction during the hydrothermal synthesis, forming a Cu → Cu_2O → CuO → LDH gradient structure, which likely helps reduce the structural and chemical discontinuity between the metallic substrate and the deposited catalyst layer. The Raman spectra of the CF

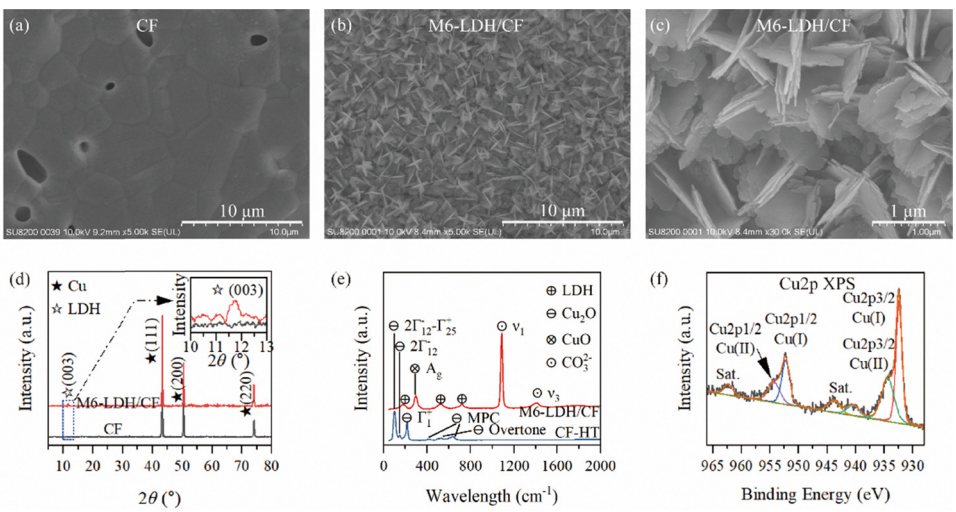

Fig. 3 SEM morphology of the CF surface, (a) before and (b) and (c) after M6-LDH growth, and (d) their XRD patterns; (e) Raman spectra of M6-LDH/CF and CF-HT, and (f) Cu 2p XPS spectra of M6-LDH/CF.

sample treated hydrothermally without adding metal nitrates (denoted as CF-HT) was used to be reference, and only the Cu_2O signal was observed, this further confirms the thermodynamic transition sequence of Cu → Cu_2O (alkaline + hydrothermal) → CuO (alkaline + oxidation + hydrothermal) on the CF surface.

3.3 Structural analysis and phase separation

XPS analysis was performed to examine the surface chemical states of the hydrothermally treated sample (Fig. 4a). In the survey spectrum, signals from all the introduced metal elements are detected, confirming the multicomponent nature of the as-obtained material (Fig. S6). In the high-resolution

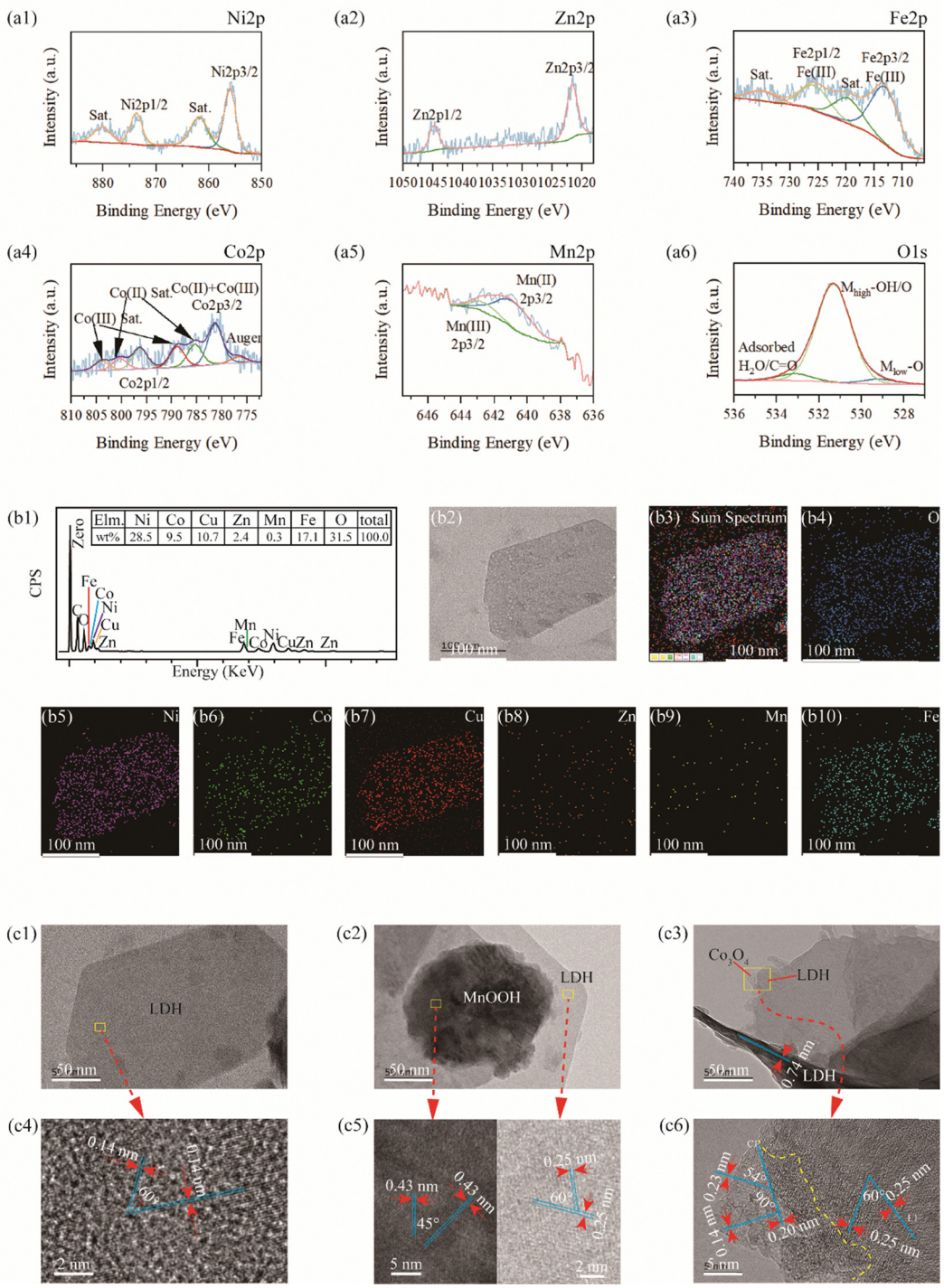

Fig. 4 Structural characterization of M6-LDH/CF: (a1)–(a6) high-resolution spectra of Ni, Zn, Fe, Co, Mn and O; (b1) EDS spectrum and elemental contents; (b2)–(b10) elemental mapping results; (c1)–(c6) representative local HRTEM observations of LDH-related domains and segregated Co/Mn-containing phases.

spectra, Ni 2p and Zn 2p exhibited characteristic peaks at 856.0 and 873.7 eV, and 1021.7 and 1044.9 eV (Fig. 4a1 and a2), corresponding to +2 metal ions in the LDH structure connected with hydroxyl groups.[28–30] Fe 2p showed characteristic peaks at 713.0 and 725.5 eV, corresponding to +3 metal ions in the LDH,[31] which form the basic framework of the material (Fig. 4a3). For Co, although the +2 and +3 peaks overlap, the broad satellite peaks (in the range of 784–791 eV) clearly indicate that two peaks are overlapped (Fig. 4a4, at 785.4 and 788.8 eV), suggesting that Co not only exists in the LDH lattice but may also exist as a separate phase.[32] For Mn (Fig. 4a5), the region of 645–650 eV overlaps significantly with the Ni LMM Auger feature in this Ni-containing multimetal LDH,[33] which should not be simply assigned to Mn(II) satellite and Mn $2p_{1/2}$. Therefore, the Mn valence state should be assessed mainly from the Mn $2p_{3/2}$ region (638–645 eV) together with other core-level spectra and complementary evidence. Two distinct peaks (640.8 and 642.6 eV) were obtained by fitting, corresponding to the oxidation states of Mn^{2+} and Mn^{3+}, respectively.[34] Since Mn^{3+} is an ion with a d^4 electron configuration, it will exhibit a strong Jahn–Teller effect in an octahedral field,[35] which may lead to its existence as a separate phase. In the O 1s spectrum (Fig. 4a6), 529.2 eV represents the bonding between low-valence metal and oxygen, which can be identified as Cu^{+}–O bonding, corresponding exactly to the previous Cu 2p XPS and Raman results; 531.3 eV corresponds to the strongest peak, attributed to the high-valence metal–O bond, corresponding to the metal–hydroxy oxygen bond in hydrotalcite, the edge unsaturated bond of LDH, and the M–O bond in the separated phase; 532.9 eV corresponds to the oxygen-containing bonds in water or other substances adsorbed on the sample surface.

Elemental mapping distribution tests were performed on the LDH flaky crystal region as shown in Fig. 4b (powder scraped from the CF substrate). The elemental contents are shown in Fig. 4b1, with the atomic ratio of Ni : Co : Cu : Zn : Mn : Fe = 1.59 : 0.53 : 0.55 : 0.12 : 0.02 : 1, deviating from the initial 0.4 : 0.4 : 0.4 : 0.4 : 0.4 : 1, especially with Mn being retained in only a small amount. All detected elements are spatially distributed within the observed region (Fig. 4b2–b10), indicating a compositionally complex multimetal system; however, this observation does not by itself imply a true high-entropy homogeneous solid solution. Significant compositional rearrangement of elements occurred, primarily due to the ''stoichiometric self-correction'' of the LDH crystal structure, where the stability of the LDH layered structure requires the molar ratio of divalent to trivalent metal ions (M^{2+}/M^{3+}) to typically range between 2.0 and 4.0. This range of layer charge densities is moderate, ensuring stability. The initial feed ratio containing Mn^{2+} had a total divalent ion-to-trivalent iron ratio of 2 : 1, but the distinct phase separation of Mn significantly reduced this value (1.6), which made the resulting LDH structure thermodynamically unstable. Therefore, in order to grow stable LDH crystals, the hydrothermal system evolved toward a more structurally compatible LDH-related composition, while chemically less compatible species were only partially retained or segregated into secondary phases.

While HRTEM provides highly localized structural information, when combined with the macroscopic phase identification from XRD, XPS, and elemental mapping, these local observations offer direct supportive evidence for the phase assemblage. Further HRTEM observations of the local region of the hexagonal platelet particles measured by Mapping (Fig. 4c1) revealed two lattice fringes (0.14 nm spacings) with a 60° angle, corresponding to the typical (110) and (1−20) crystal planes in LDH (Fig. 4c4). In another local region, circular particles were found to be loaded on the hexagonal platelet particles (Fig. 4c2). HRTEM analysis revealed two lattice fringes with a 60° angle and a 0.25 nm spacings on the hexagonal platelets, corresponding to the typical (100) and (010) crystal planes in LDH, while on the circular particles, two lattice fringes with a 45° angle and a 0.43 nm spacing were observed, corresponding to the (110) and (1−10) crystal planes of α-MnOOH (Fig. 4c5). These crystal planes with distinct angles and spacings provide local microstructural evidence that the independently phase-separated α-MnOOH particles are loaded onto the multimetal LDH nanosheets.

In another typical region, side-standing LDH was observed, positioned on top of another flat-lying platelet particle. The side-standing LDH was confirmed by a 0.74 nm spacing, which is uncommon in other materials (Fig. 4c3), corresponding to the (003) crystal plane. In the HRTEM observation of the edge of the flat-lying platelet particle, two distinct phases were found to be stacked: in the left region, three sets of crystal planes with spacings of 0.14, 0.20, and 0.23 nm were observed, with angles of 90° and 54° between the first set and the other two, corresponding to the (044), (400), and (222) crystal planes of Co_3O_4, which supports the presence of a Co-containing oxide phase in this local region. On the right side, the large flat platelet particles showed two lattice fringes with a 60° angle and a 0.25 nm spacings, corresponding to the (1−10) and (−100) crystal planes of LDH. The flat-lying and side-standing LDH further confirm the ''house-of-cards'' morphology with cross-supporting structures observed in the SEM images.

The deviation of each component from the initial feed amount in the EDS and XPS results is a direct result of the significant differences in the precipitation kinetics of each element in the alkaline hydrothermal environment. The pH environment created by urea hydrolysis is very conducive to the precipitation and crystallization of Ni^{2+}, which almost entirely enters the LDH lattice and becomes the main framework of the layered structure, resulting in its higher content. Zn^{2+} tends to form tetrahedral coordination, but the octahedral coordination requirement of the LDH layers creates insufficient driving force for Zn to enter the lattice. Additionally, Zn^{2+} can combine with OH^{-} to form soluble zincate ions $[Zn(OH)_4]^{2-}$, causing most of the Zn to dissolve into the solution. Ammonia gas has a clear complexing and dissolving effect on Cu, so theoretically, Cu should also be lost. However, the substrate releases additional copper in the hydrothermal environment, and eventually, part of the Cu enters the LDH lattice, while some forms Cu_2O/CuO interfaces, leading to a final content slightly higher than the initial feed amount.

Co^{2+} can only form a small amount of complexes, so based on the Mapping, XPS, and TEM results, most of it remains in the lattice, with a small amount existing as an oxide. Due to significant differences in oxidation kinetics, Mn^{2+} is easily further oxidized to Mn^{3+} or Mn^{4+}. Mn^{3+} is a strong Jahn–Teller ion that causes severe lattice distortion in the LDH, making it difficult to coexist stably with Fe, Ni, and other elements in large amounts. This forces the remaining Mn to crystallize separately outside, such as forming MnOOH. Mn^{4+} easily forms extremely small MnO_2 colloids, which, if not adsorbed onto the copper foam, will remain suspended in the solution and be washed away. If the independent Mn phase and dissolved Zn content are excluded, the initial M^{2+}/M^{3+} ratio would be much less than 1.6 : 1, so the amount of Fe^{3+} added during the feed is in excess of what is needed to form the LDH. This excess Fe cannot enter the lattice, and if the formed hydroxide cannot adhere to the copper foam, it may be washed away during the cleaning process.

3.4 OER performance and electrochemical evaluation

The OER and electrochemical evaluation results of sample with different numbers of components are shown in Fig. 5 while Table S1 in SI collects the overpotentials at various current densities for all the samples. LSV tests indicate that CF has the weakest electrochemical activity, with corresponding overpotentials of 333 mV and 548 mV at current densities of 10 and 50 mA cm^{-2}, respectively (Fig. 5a and b). As the number of components in the LDH formed on the CF surface gradually increases, the current density increases and the overpotentials decrease. The six-component sample (M6-LDH/CF) exhibits the best performance, with overpotentials of only 181, 392 and 502 mV at current densities of 10, 50 and 100 mA cm^{-2}, respectively. It should be noted that for transition-metal hydroxide/oxide-based precatalysts, the low-potential region of the anodic polarization curve (*e.g.*, around the onset and 10 mA cm^{-2}) may include mixed contributions from metal oxidation/activation processes in addition to the OER current. Therefore, the superior performance of M6-LDH/CF is more conclusively demonstrated at higher current densities (such as 50 and 100 mA cm^{-2}), where the OER process dictates the current response. This finding suggests that the integrated multicomponent architecture, derived from kinetically competitive *in situ* growth, provides a clear advantage over lower-component controls.

To elucidate the role of the substrate, LDH powder was synthesized separately and adhered to CF using Nafion solution to obtain M6-LDH-P/CF. The performance of this sample was found to be poor, only slightly better than CF, and even lower than the binary NiFe M2-LDH/CF system. This suggests that simply adhering M6-LDH powder to the substrate, cannot leverage advantages of the integrated architecture, due to high interface contact resistance and lack of strong binding. The superior performance of the *in situ* sample is associated with the Cu-derived interfacial transition region, which likely promotes stronger catalyst–substrate coupling and lower interfacial resistance than the physically coated powder electrode.

The apparent Tafel slope values derived from the polarization curves for CF, M6-LDH-P/CF, M2-LDH/CF, M3-LDH/CF, M4-LDH/CF, M5-LDH/CF, and M6-LDH/CF samples are 212.3, 140.2, 112.6, 104.7, 95.3, 83.6, and 74.6 mV dec^{-1}, respectively, indicating that the increase in components significantly improves the apparent OER kinetics (Fig. 5c). Co or Mn species typically exhibit favorable OER kinetics, and their incorporation (even in the form of segregated phases) is widely reported in the literature to be beneficial for lowering anodic energy barriers.[36–39] Therefore, the MnOOH- and Co_3O_4-containing segregated phases are discussed here as likely contributing domains that may, together with the multimetal LDH framework, promote the overall surface reactivity of M6-LDH/CF, rather than acting as solely isolated active centers.

EIS measurements were conducted using an equivalent circuit consisting of a resistor in series with a parallel resistor–capacitor element. The charge transfer resistance values for the samples were determined to be 20.1, 17.46, 12.4, 12.2, 12.0, 6.1, and 3.4 Ω, respectively (Fig. 5d). It can be observed that the resistance of M5-LDH/CF (containing Co) is halved compared to M4-LDH/CF, while the resistance of M6-LDH/CF (containing Mn) is further halved, suggesting that the Co/Mn-containing segregated surface phases, together with the integrated electrode architecture, are associated with improved interfacial charge-transfer behavior. Additionally, the p-type semiconductor properties of the CuO interlayer and the n-type semiconductor properties of the LDH form a junction effect, which may also facilitate interfacial electron transfer.

The double-layer capacitance (C_{dl}) values for the samples are 3.1, 5.5, 5.7, 6.3, 7.4, 10.8, and 14.1 mF cm^2, respectively (Fig. 5e and Fig. S7). The significant change in C_{dl} from binary to multicomponent systems may be associated with nanoparticle decoration, multicomponent phase organization, and defect-rich surface features. $MnOOH/Co_3O_4$ nanoparticles, as observed in TEM, decorate the surface of the LDH nanosheets, which directly increases the electrochemical active surface area (ECSA). While the lattice distortion and phase-separation interfaces induced by multimetal doping provide additional accessible active sites. To further elucidate the origin of the performance enhancement, ECSA-normalized polarization curves were plotted (Fig. 5f). The normalized results show that M6-LDH/CF does not exhibit the highest apparent intrinsic activity per unit ECSA among the tested samples. This indicates that the superior performance of M6-LDH/CF on a geometric-area basis is primarily associated with its much larger electrochemically accessible surface area and the integrated electrode architecture formed during *in situ* growth, rather than a uniform enhancement of intrinsic activity. At the same time, because the ECSA in the present system is estimated from C_{dl} for a multicomponent porous Cu-foam-supported electrode, the normalized results should still be interpreted cautiously as approximate descriptors rather than absolute intrinsic-activity metrics.

To evaluate the operational stability of the catalyst, chronopotentiometric testing was carried out at a current density of 50 mA cm^{-2} (Fig. 5g). The M6-LDH/CF electrode can maintain

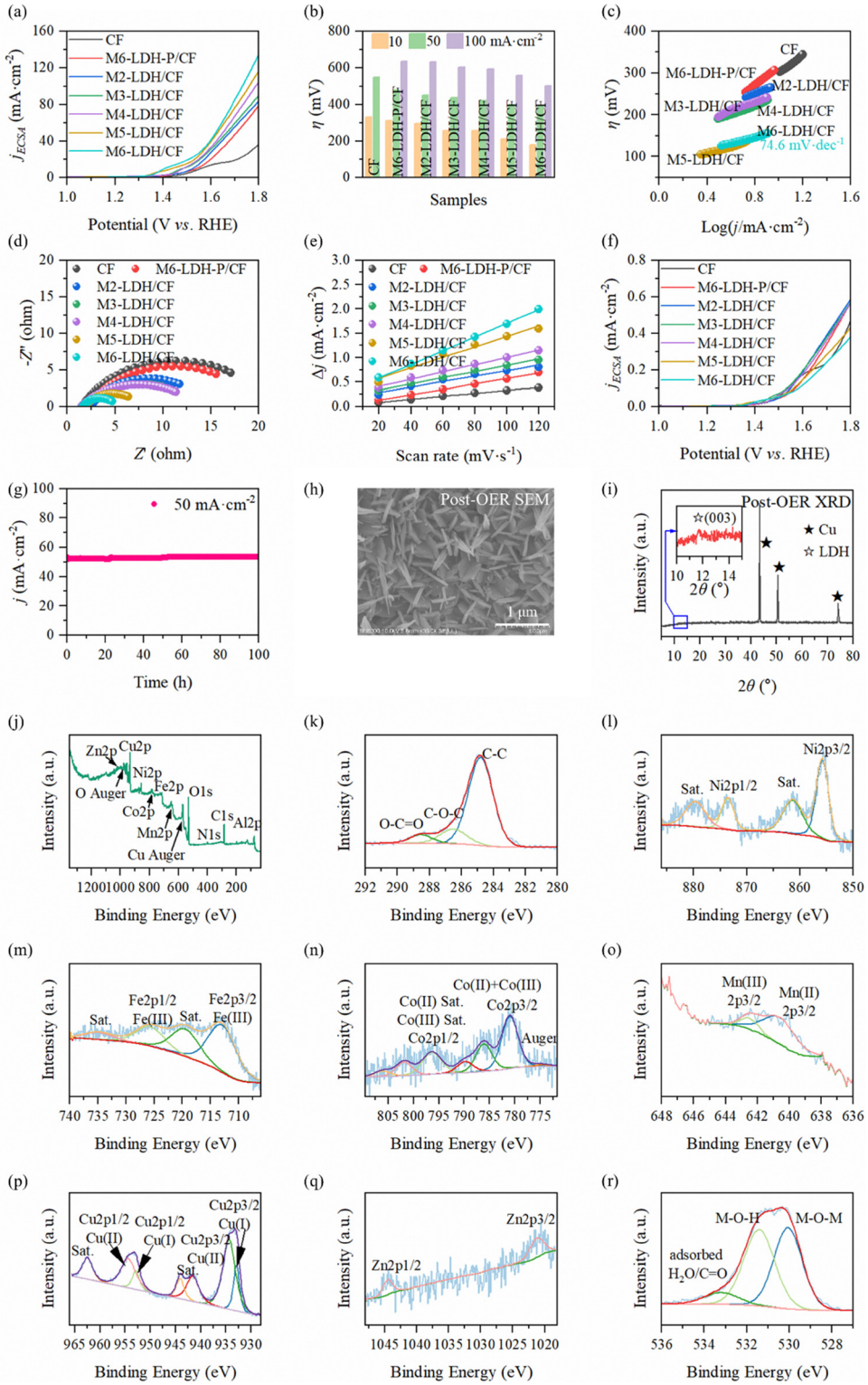

Fig. 5 Electrochemical performance of the samples: (a) LSV curves, (b) overpotentials at current densities of 10, 50 and 100 mA cm^{-2}, (c) Tafel slopes, (d) EIS plots, (e) C_{dl} fitting curves, (f) ECSA-normalized polarization curves, (g) long-term stability test of M6-LDH/CF, and post-OER (h) SEM, (i) XRD and (j)–(r) XPS.

continuous anodic operation under this condition for 100 h, indicating that the directly grown integrated electrode architecture is sufficiently stable for sustained OER testing. Post-OER SEM and XRD characterizations further provide insight into the structural evolution of the electrode after prolonged operation (Fig. 5h and i). SEM images show that the nanosheet

domains remain on the substrate after the stability test, but their lateral size becomes smaller and their thickness increases, while the initially pronounced exfoliated or delaminated features become less obvious. This suggests that the LDH-derived nanosheets do not collapse completely during OER, but instead undergo partial reorganization and densification under anodic conditions. Consistently, the post-OER XRD pattern still retains the characteristic LDH (003) reflection, indicating that the layered host framework is not fully destroyed during OER, even though significant surface and morphological evolution occurs.

Post-OER XPS (Fig. 5j–r) further reveals pronounced surface-state reconstruction after 100 h operation. In the Cu 2p spectrum, the Cu^{+}-related component decreases markedly, accompanied by a shift toward a more Cu^{2+}-dominated Cu–O/OH environment, indicating further oxidation of Cu-containing species under OER conditions. At the same time, the Zn signal becomes significantly weaker, which is consistent with selective Zn leaching in strongly alkaline anodic media. Such Zn dissolution is expected to generate cation vacancies and perturb the local electronic environment of neighboring metal centers. In addition, the O 1s spectrum shows a clear enhancement of the metal–oxygen–metal component, indicating the formation of more oxide/oxo-bridged coordination environments. This evolution is likely associated not only with oxidation of Cu^{+} to Cu^{2+}, but also with dehydroxylation/condensation within the LDH-derived layers. Taken together, these results show that M6-LDH/CF does not remain chemically invariant during operation, but instead evolves toward a more oxidized working state.

By combining the post-OER SEM, XRD, and XPS results, it can be concluded that the catalyst undergoes a ''framework-retained but surface-reconstructed'' evolution during OER. In other words, the LDH-derived layered skeleton is still partially preserved, whereas the nanosheet morphology becomes more compact and the surface coordination environment shifts from a hydroxyl-rich mixed-valence state toward a more oxide/oxo-bridged and oxidized state. Accordingly, M6-LDH/CF is more appropriately described as a precatalyst architecture, whose initial integrated phase organization and substrate coupling support favorable anodic performance and operational stability, while the surface chemistry and local morphology evolve during prolonged OER.

The improved anodic behavior of M6-LDH/CF is therefore interpreted as the combined result of several structural and interfacial factors. The six-metal LDH nanosheet framework provides a compositionally complex host matrix and a large accessible surface area; the segregated Co/Mn-containing surface phases are considered likely catalytically relevant domains; and the reconstructed $Cu/Cu_2O/CuO$ interfacial region promotes strong catalyst–substrate integration. Based on the present *ex situ* evidence and structure–performance correlation, these segregated phases are discussed here as likely contributors to the enhanced OER behavior, rather than as conclusively identified active centers. This interpretation is also consistent with previous reports showing that MnOOH- and Co_3O_4-based phases can be catalytically relevant under alkaline OER conditions.[36–39]

Taken together, the electrochemical and post-OER characterization results indicate that the superior performance of M6-LDH/CF arises not from a single isolated factor, but from the coupling of enlarged accessible surface area, favorable phase organization, strong catalyst–substrate integration, and a reconstruction pathway enabled by the initial precatalyst architecture.

3.5 Transformation thermodynamics of CF surfaces in alkaline hydrothermal environments and its lattice matching with M6-LDH

In the synthesis of the M6-LDH/CF sample, the initial concentration of nitrate ions was 0.175 mol L^{-1}, and the initial concentration of urea was 0.3 mol L^{-1}. Under such conditions, nitrate ions were used as the oxidizing agent to perform a non-standard thermodynamic derivation of the oxidation process of CF at 120 °C. The two-stage redox reaction equations are as follows:

Stage I ($Cu \rightarrow Cu_2O$):

$$2Cu(s) + NO_3^-(aq) + H_2O(l) \rightarrow Cu_2O(s) + NO_2^-(aq) + 2OH^-(aq)$$

Stage II ($Cu_2O \rightarrow CuO$):

$$Cu_2O(s) + NO_3^-(aq) + H_2O(l) \rightarrow 2CuO(s) + NO_2^-(aq) + 2OH^-(aq)$$

The formation free energy of each species at 298.15 K was obtained from the thermodynamic database (see Table S2), and the standard free energy change at 393.15 K was derived using the formula $\Delta G = \Delta G_T^0 + RT\ln Q$ as indicated in the SI resulting in:

$$\Delta G_I = -192.4 \text{ kJ mol}^{-1}$$

$$\Delta G_{II} = -162.4 \text{ kJ mol}^{-1}$$

Therefore, thermodynamics indicates that at a concentration of 0.175 mol L^{-1} of nitrate ions, the ΔG values for both stages are significantly negative, confirming that at 120 °C, nitrate ions provide sufficient chemical potential to drive the oxidation of copper. The free energy change for Stage I is more negative than for Stage II, suggesting a stronger thermodynamic tendency for the initial transformation from Cu to Cu_2O, which accelerates the densification and growth of the Cu_2O layer at the interface. The free energy difference of approximately 30 kJ mol^{-1} between Stage I and Stage II ensures the existence of a $Cu/Cu_2O/CuO$ gradient layer at the interface, which provides a plausible thermodynamic basis for the subsequent *in situ* growth and interfacial integration of the multi-metal LDH-based catalyst layer, which is likely beneficial for the observed operational stability under the tested conditions.

To further understand why the catalyst layer can be formed stably on the Cu foam substrate, the compatibility between LDH and the substrate was examined. This was mainly considered from both geometric and chemical perspectives.

In the geometric perspective, the lattice mismatch, δ, between different surfaces (Cu, Cu_2O, CuO) and the typical crystal planes of LDH was used to evaluate the degree of structural compatibility:

$$\delta = \frac{|d_{Sub} - d_{LDH}|}{d_{Sub}}$$

where d_{sub} is the lattice spacing of the substrate, and d_{LDH} is the lattice spacing of the LDH that grew *in situ*. If $\delta < 5\%$, the lattice matching is considered favorable for interfacial accommodation and stable catalyst growth. If $\delta > 5\%$, there is significant lattice strain, weak interfacial bonding, and a higher likelihood of defects or detachment.[40–42]

First, the characteristic crystal plane relevant to the LDH-related phase was considered. As shown in the SEM observations (Fig. 2 and 3), the nanosheets formed on the substrate are predominantly arranged in an approximately vertical orientation, which is commonly observed for directly grown layered nanosheet arrays on conductive foams.[43,44] Under this growth mode, the (100) and related in-plane crystal phase, with an interplanar spacing of about 0.25 nm, are the most relevant structural motifs for evaluating matching with the substrate. Therefore, the LDH (100)-type plane was selected as primary anchoring plane to find the most suitable matching substrate plane.

Metallic Cu has a face-centered cubic (FCC) structure, and the lattice spacing of the (111) plane is approximately 0.20 nm, which is closest to the selected LDH anchoring crystal plane (100) (Fig. 6). The lattice mismatch between Cu (100) and the (100) or (010) crystal planes of LDH is 25%. This suggests that direct structural accommodation between metallic Cu and the LDH phase is not ideal. In addition, the bonding characteristics of metallic Cu differ substantially from those of hydroxide-based layered compounds, making the direct nucleation and stable growth of the LDH-related phase on bare Cu less favorable.

Cu_2O has a cubic crystal structure,[45] with the (111) crystal plane spacing of 0.246 nm, which is very close to that of LDH, with a lattice mismatch of only 1.6% compared to the LDH (100) or (010) crystal planes, indicating a good match (Fig. 6). However, in Cu_2O, Cu is in the +1 oxidation state, while LDH layers require M^{2+} and M^{3+} hydroxyl coordination;[46,47] Moreover, the oxygen coordination environment in Cu_2O differs significantly from the octahedral coordination of LDH. Therefore, Cu_2O serves as a good transition layer, but its binding strength is not as strong as that of CuO.

CuO has a monoclinic crystal structure, with the main crystal planes being (−111) or (002), and the lattice spacing is approximately 0.252 nm. The lattice mismatch between the (100) or (010) crystal planes of LDH and these planes is only 0.8%, indicating a very good match. Additionally, the M–O octahedral distribution in LDH is similar to the Cu–O octahedral arrangement in CuO.[46] Therefore, the characteristic crystal planes of CuO and the growth crystal planes of LDH are highly coincident in terms of geometric dimensions, making it very easy to form a low-energy, either coherent or semi-coherent interface.

More importantly, the comparison in the chemical dimension highlights the advantages of the interaction between LDH and CuO: the surface of metallic Cu is hydrophobic, making it difficult to form –OH bonds; in contrast, CuO readily undergoes a hydration reaction in the alkaline hydrothermal environment, as described by the equation $CuO + H_2O \rightarrow Cu(OH)_{surf}$, forming a Cu–OH structure on its surface. This Cu–OH structure is chemically homologous to the M–OH octahedral structure in the LDH layers.[48] Therefore, the diverse metal ions in the multimetal LDH (Ni, Fe, Zn, Co, Mn) can easily anchor to the CuO surface through an "olation" (hydroxyl-bridge bonding) reaction. Additionally, the crystal structure of CuO consists of CuO_4 planes sharing edges and corners, which, compared to the three-dimensional network structure of Cu_2O, more closely resembles the layered topological features of LDH, making it favorable for inducing the nucleation of layered materials, thereby ensuring the robust interfacial coupling and mechanical stability of the integrated M6-LDH/CF precatalyst architecture.[49]

3.7 Structural model

Based on the above structural, thermodynamic, and electrochemical results, a schematic model of the M6-LDH/CF electrode can be proposed, as illustrated in Fig. 7.

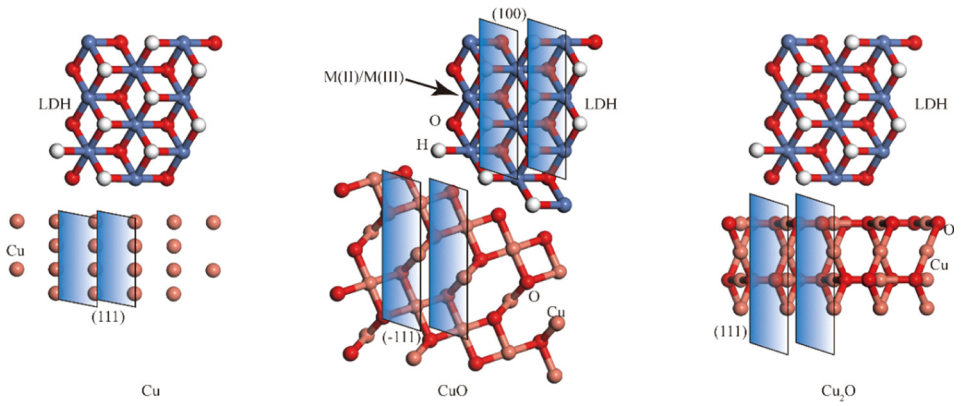

Fig. 6 Schematic diagram of LDH matched with different substrates.

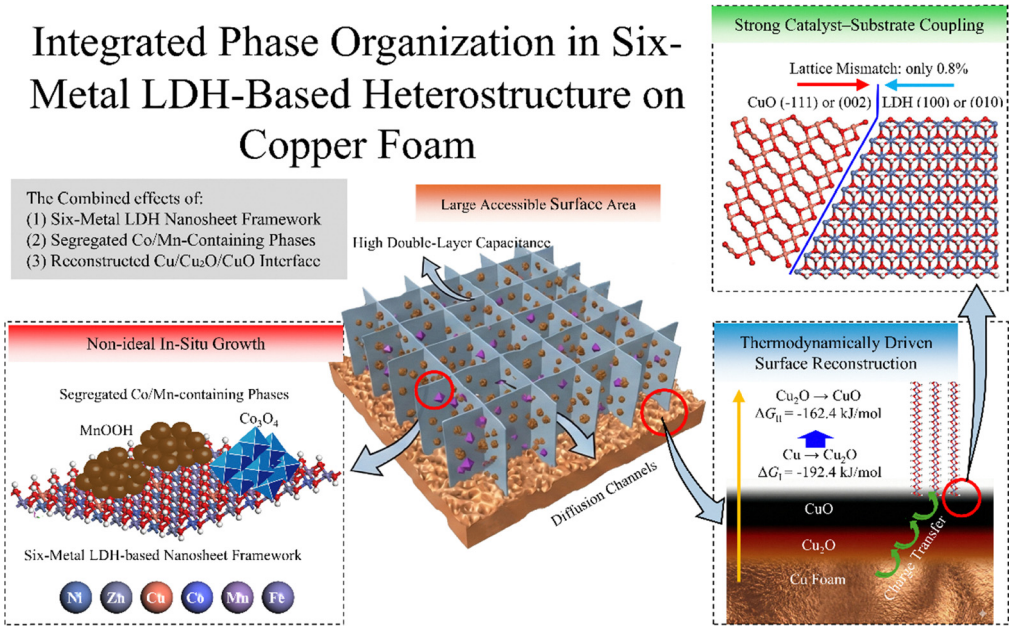

Fig. 7 Schematic illustration of integrated phase organization in M6-LDH/CF.

During one-step hydrothermal growth on copper foam, the precursor system does not evolve into an ideal homogeneous multimetal LDH phase. Instead, owing to the different hydrolysis, oxidation, and precipitation behaviors of the metal ions, together with the simultaneous oxidation and reconstruction of the Cu substrate, the system develops into an integrated multicomponent architecture consisting of a six-metal LDH nanosheet framework, segregated Co/Mn-containing surface phases, and a $Cu/Cu_2O/CuO$-derived interfacial region.

On the macroscopic scale, the optimized synthesis conditions (120 °C, 12 h, $U/M^{2+} = 6:1$) induce the nanosheets to grow in a vertically supported and interlaced manner, forming an open three-dimensional "house-of-cards" array. This architecture contributes to a high double-layer capacitance and provides abundant accessible surface area, while also creating channels that are favorable for electrolyte penetration, reactant diffusion, and O_2 bubble release. These structural features help explain why the directly grown M6-LDH/CF exhibits much better geometric-area-based anodic performance than the physically coated M6-LDH-P/CF sample.

On the microscopic scale, the present study suggests that the non-ideal growth behavior of the multimetal precursor system plays a constructive role in determining the final electrode structure. While Ni-, Fe-, and part of the other metal species contribute to the LDH-related host framework, the chemically less compatible fractions of Co and Mn tend to segregate and form secondary surface phases. At the same time, the Cu substrate undergoes stepwise reconstruction, producing a $Cu/Cu_2O/CuO$ interfacial transition region that is both geometrically and chemically more compatible with the LDH-related catalyst layer than metallic Cu alone. As discussed in Sections 3.5 and 3.6, this interfacial evolution provides a plausible structural basis for strong catalyst–substrate coupling and favorable charge-transfer pathways in the directly grown electrode.

The superior performance of M6-LDH/CF is therefore not attributed to a single isolated factor. Rather, it is more reasonably understood as arising from the combined effects of: (i) a six-metal LDH-based nanosheet framework that provides a compositionally complex host matrix and a large accessible surface area; (ii) segregated Co/Mn-containing surface phases that likely serve as catalytically relevant domains; and (iii) a reconstructed $Cu/Cu_2O/CuO$ interfacial region that enhances catalyst–substrate integration and facilitates interfacial charge transfer.

It should also be emphasized that the present model does not imply that the as-synthesized structure remains fully unchanged during OER. Combined with the post-OER XPS results, M6-LDH/CF is more appropriately described as a pre-catalyst architecture: its initial phase organization and interfacial coupling help establish a favorable working electrode, while the surface chemistry evolves toward a more oxidized state under prolonged anodic operation. Therefore, the role of the initial architecture is not to remain structurally invariant, but to influence the accessible catalytic domains, interfacial transport, and likely reconstruction pathway during OER.

Overall, the excellent anodic performance of M6-LDH/CF is associated with the integrated phase organization produced by non-ideal *in situ* growth, including enlarged accessible surface area, favorable interfacial matching, strong catalyst–substrate coupling, and a precursor structure that can evolve into an electrochemically effective working state during OER.

4. Conclusion

In summary, a six-metal NiZnCuCoMnFe LDH-based heterostructure was constructed directly on copper foam through a one-step hydrothermal process. Rather than yielding an ideal

homogeneous multimetal LDH phase, the actual synthesis pathway produced an integrated architecture composed of a six-metal LDH nanosheet framework, segregated Co/Mn-containing surface phases, and a reconstructed $Cu/Cu_2O/CuO$ interfacial region. This result highlights that, during *in situ* growth on an active metallic substrate, differences in cation hydrolysis, oxidation, and precipitation behavior can drive a non-ideal yet structurally integrated phase organization.

The optimized M6-LDH/CF electrode exhibits improved anodic OER performance compared with the lower-component controls and the physically coated powder electrode, reflecting the beneficial role of enlarged accessible surface area, favorable phase organization, and strong catalyst–substrate coupling. Electrochemical analysis indicates that its superior geometric-current performance is primarily associated with the integrated electrode architecture formed during *in situ* growth, rather than being attributed solely to a uniformly enhanced intrinsic activity of all exposed surface sites.

Post-OER XPS further shows that the catalyst surface undergoes clear chemical evolution during prolonged anodic operation, including Cu oxidation, Zn leaching, and the formation of more metal–oxygen–metal coordination environments. These results suggest that M6-LDH/CF functions as a precatalyst architecture, whose initial phase organization and interfacial integration help support stable operation under the tested conditions while the surface evolves toward a more oxidized working state during OER.

Overall, this work suggests that controlled non-ideal growth and spontaneous phase segregation can be used constructively to fabricate integrated multimetal OER electrodes on conductive substrates. Rather than emphasizing the formation of an idealized high-entropy solid solution, the present study highlights the importance of understanding the real structure actually obtained during *in situ* synthesis and its relationship to electrocatalytic behavior in alkaline media. This study provides a practical perspective for designing multicomponent alkaline OER electrodes by coupling compositional complexity, phase organization, and substrate-derived interfacial reconstruction within a single integrated architecture.

Conflicts of interest

There are no conflicts to declare.

Data availability

The data supporting this study are available within the article and its supplementary information (SI). Supplementary information: electrochemical performance test results of samples with different synthesis conditions and different numbers of metal members, Raman spectrum of copper foam, XPS survey spectrum of M6-LDH/CF, comparison of overpotential of different samples under three current densities, calculation process of free energy of copper substrate and the required basic thermodynamic parameters for the two-stage oxidation process of copper substrate under alkaline conditions. See DOI: https://doi.org/10.1039/d6ey00071a.

Acknowledgements

This work was funded by the National Natural Science Foundation of China (52020105011), the China University of Mining and Technology (CUMT) Open Sharing Fund for Large-scale Instruments and Equipment (DYGX-2025-63), and the Jiangsu Key Laboratory for Clean Utilization of Carbon Resources (BM2024007). Funding by the Spanish Agencia Estatal de Investigación (CEX-2021-001230-S and PID2024-161014 NB-I00 funded by MCIN/AEI/10.13039/501100011033) and the Generalitat Valenciana (CIPROM/2024/071) is also gratefully acknowledged.

References

1 M. G. Walter, E. L. Warren, J. R. McKone, S. W. Boettcher, Q. Mi, E. A. Santori and N. S. Lewis, *Chem. Rev.*, 2010, **110**, 6446–6473.
2 T. R. Cook, D. K. Dogutan, S. Y. Reece, Y. Surendranath, T. S. Teets and D. G. Nocera, *Chem. Rev.*, 2010, **110**, 6474–6502.
3 J. G. Segovia-Hernández, S. Hernández, E. Cossío-Vargas, M. Juarez-García and E. Sánchez-Ramírez, *RSC Sustainability*, 2025, **3**, 134–157.
4 J. Wang, Y. Gao, H. Kong, J. Kim, S. Choi, F. Ciucci, Y. Hao, S. Yang, Z. Shao and J. Lim, *Chem. Soc. Rev.*, 2020, **49**, 9154–9196.
5 Z. W. Seh, J. Kibsgaard, C. F. Dickens, I. Chorkendorff, J. K. Nørskov and T. F. Jaramillo, *Science*, 2017, **355**, eaad4998.
6 N.-T. Suen, S.-F. Hung, Q. Quan, N. Zhang, Y.-J. Xu and H. M. Chen, *Chem. Soc. Rev.*, 2017, **46**, 337–365.
7 F. Song and X. Hu, *Nat. Commun.*, 2014, **5**, 4477.
8 L. Sun, J. Niu, H. Liu, F. Liu, A. A. Reka, J. Matusik and P. Feng, *RSC Sustainability*, 2025, **3**, 715–737.
9 J. Xie, C. Li, J. Niu, S. Zhang, X. Ou, P. Feng and H. Garcia, *Mater. Lett.*, 2021, **290**, 129517.
10 Y. Luo, L. Sun, J. Niu, M. Zhi, C. Yao, H. Liu, F. Liu, A. A. Reka, F. Akhtar and P. Feng, *Mater. Lett.*, 2025, 139118.
11 Q. Wang and D. O'Hare, *Chem. Rev.*, 2012, **112**, 4124–4155.
12 Y. Liu, Y. Wen, X. Liu, G. Xu, C. Bao, X. Yang and L. Li, *Chem. Commun.*, 2026, DOI: 10.1039/D6CC00168H.
13 X. Duan, M. G. Sendeku, D. Zhang, D. Zhou, L. Xu, X. Gao, A. Chen, Y. Kuang and X. Sun, *Acta Phys.-Chim. Sin.*, 2024, **40**, 2303055.
14 Z. Jin, Z. Cao, L. Jin, S. Ding and K. Xi, *Nano-Micro Lett.*, 2026, **18**, 200.
15 B. Singh, S. Verma, A. Goyal, A. Yadav, L. Singh, V. Varshney, R. Singh, A. Singh and A. Draksharapu, *Chem. Commun.*, 2026, **62**, 3116–3141.
16 Y. Liu, X. Jiao, Y. Li, C. Shi, X. Jiang, X. Qi, C. Xing, X. Wang and A. Cabot, *Sci. China Mater.*, 2026, 1–9.
17 L. Sun, Y. Zeng, J. Li, H. Wang, Q. Hua and S. Lu, *Langmuir*, 2025, **41**, 1539–1546.

18 X. Lu, H. Xue, H. Gong, M. Bai, D. Tang, R. Ma and T. Sasaki, *Nano-Micro Lett.*, 2020, **12**, 86.
19 M. Bukhtiyarova, *J. Solid State Chem.*, 2019, **269**, 494–506.
20 Z. Li, S. Zhang, M. Cao, S. Li, X. Lou, H. Yang, P. Xu, J. Chen and Q. Zhang, *ACS Nano*, 2026, **20**, 4942–4952.
21 X. Wang, Q. Yang, L. Wang, M. Zhang, B. Dong, S. Hong, S. MacKay and X. Zhang, *Adv. Compos. Hybrid Mater.*, 2026, **9**, 82.
22 H. Yang, C. Dong, H. Wang, R. Qi, L. Gong, Y. Lu, C. He, S. Chen, B. You and H. Liu, *Proc. Natl. Acad. Sci. U. S. A.*, 2022, **119**, e2202812119.
23 C. Zhang, J. Wang, H. Ma, J. Wang, R. Xu, G. Li, L. Yang and H. Guo, *Chem. Eng. J.*, 2024, **499**, 156430.
24 H. Sun, H. Kim, S. Song and W. Jung, *Mater. Rep.: Energy*, 2022, **2**, 100092.
25 D. He, G. Wang, G. Liu, H. Suo and C. Zhao, *Dalton Trans.*, 2017, **46**, 3318–3324.
26 M. Liu, N. Li, S. Meng, S. Yang, B. Jing, J. Zhang, J. Jiang, S. Qiu and F. Deng, *J. Hazard. Mater.*, 2024, **478**, 135484.
27 B. Chen, Z. Zhang, S. Kim, S. Lee, J. Lee, W. Kim and K. Yong, *ACS Appl. Mater. Interfaces*, 2018, **10**, 44518–44526.
28 H. Yang, S. Luo, Y. Bao, Y. Luo, J. Jin and J. Ma, *Inorg. Chem. Front.*, 2017, **4**, 1173–1181.
29 J. He, P. Xu and J. Sun, *ACS Sustainable Chem. Eng.*, 2020, **8**, 2931–2938.
30 M. C. O'Brien and C. Chancey, *Am. J. Phys.*, 1993, **61**, 688–697.
31 J. Chen, Y. Sun, Z. Li, G. Yuan and G. Han, *New J. Chem.*, 2025, **49**, 9990–9997.
32 C. Li, Z. Chen, W. Yuan, Q.-H. Xu and C. M. Li, *Nanoscale*, 2019, **11**, 1111–1122.
33 Q. Ke, C. Guan, M. Zheng, Y. Hu, K.-H. Ho and J. Wang, *J. Mater. Chem. A*, 2015, **3**, 9538–9542.
34 S. Gong, M. Zhu, Y. Zhou, R. Li, J. Zhang, X. Jia, D. Chao and C. Wang, *Chem. Sci.*, 2024, **15**, 19870–19885.
35 Z. Zhang, J. Zheng, X. Chen, X. Yu, L. Li, L. Bao, J. Peng and X. Li, *Energy Storage Mater.*, 2025, **76**, 104128.
36 Y. Li, F.-M. Li, X.-Y. Meng, S.-N. Li, J.-H. Zeng and Y. Chen, *ACS Catal.*, 2018, **8**, 1913–1920.
37 F. H. Lima, M. L. Calegaro and E. A. Ticianelli, *Electrochim. Acta*, 2007, **52**, 3732–3738.
38 X. Li, J. Wang, H. Xue, L. Zhao, J. Lu, H. Zhang, M. Yan, F. Deng and C. Hu, *Adv. Funct. Mater.*, 2025, **35**, 2503360.
39 C. Cui, G. Du, K. Zhang, T. An, B. Li, X. Liu and Z. Liu, *J. Alloys Compd.*, 2020, **814**, 152239.
40 Y. Du, B. Xu, G. Wang, Y. Miao, B. Li, Z. Kong, Y. Dong, W. Wang and H. H. Radamson, *Nanomaterials*, 2022, **12**, 741.
41 K. Huang, R.-J. Huang, S.-Q. Liu and Z. He, *J. Electrochem.*, 2022, **28**, 2213006.
42 A. Giri, G. Park and U. Jeong, *Chem. Rev.*, 2023, **123**, 3329–3442.
43 Y. Li, F. Gianfreda, C. Danesi, P. Bollero, A. Ermini, R. Pizzoferrato and E. Nicolai, *Crystals*, 2023, **13**, 1636.
44 J. Hu, Y. Zhang and M. Dong, *Adv. Funct. Mater.*, 2024, **34**, 2312452.
45 R. Dahal, S. K. Ray, G. Pathiraja and B. P. Bastakoti, *J. Mater. Sci.*, 2024, **59**, 13896–13907.
46 T. Zhu, B. Wu, J. Xie, H. Yang, W. Zhang and Y. Sun, *ACS Sustainable Chem. Eng.*, 2023, **11**, 17482–17491.
47 L. Li, Q. Cao, X. Dong, X. Yu, H. Yao, S. Zeng and X. Guo, *Sci. China Mater.*, 2025, **68**, 2742–2748.
48 R. Chandiramouli, S. Subramanian and S. Valantina, *Mater. Sci.*, 2015, **21**, 173–178.
49 Y. Sun, J. Mi, L. Li, S. Yu, S. Yuan, G. Wang, J. Chen and J. Li, *Catal. Commun.*, 2024, **187**, 106880.